Electronic Supplementary Material (ESI) for Dalton Transactions.

Bimetallic CPM-37(Ni,Fe) metal-organic framework: enhanced porosity, stability and tunable composition

Soheil Abdpour, Marcus. N. A. Fetzer, Robert Oestreich, Thi Hai Yen Beglau, István Boldog* and Christoph Janiak*

Institut für Anorganische Chemie und Strukturchemie, Heinrich-Heine-Universität Düsseldorf, 40204 Düsseldorf, Germany

soheil.abdpour@hhu.de, marcus.fetzer@uni-duesseldorf.de, robert.oestreich@uni-duesseldorf.de, beglau@uni-duesseldorf.de, boldogi@hhu.de, janiak@hhu.de

Contents

Section 1 Synthesis

Section 1.1 Synthesis of N,N',N"-tris-(pyrid-4-yl)-trimesamide (TPAMA)

Materials used

3A molecular sieves (CAS: 308080-99-1), tetrahydrofuran, THF (CAS: 109-99-9, anhydrous, ≥99.9%), 1,3,5-benzene tricarboxytrichloride (CAS: 4422-95-1, 98%), and triethylamine (CAS:121-44-8, 99.5%) were purchased from Merck GmbH, 4-aminopyridine (CAS: 504-24-5, 98%), dimethylsulfoxide, DMSO (CAS: 67-68-5 99%), and acetone (CAS: 67-64-1, ACS reagent, ≥99.5%) from Thermo Fisher Scientific. All solvents were dried over molecular sieves. Prior to use, THF and triethylamine were freshly distilled. Unless otherwise described, all reactions were carried out under nitrogen atmosphere.

Synthesis

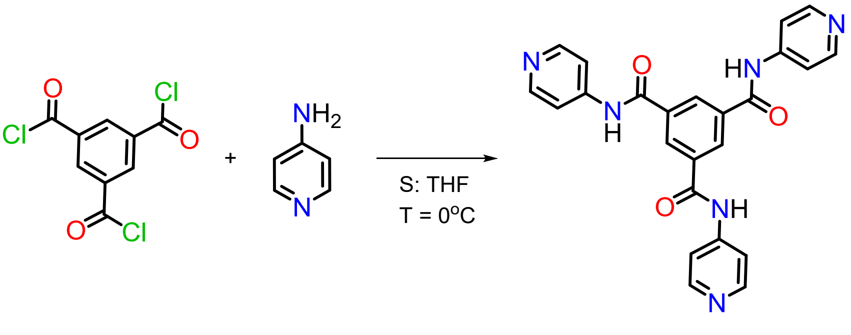

TPAMA

The TPAMA ligand was synthesized according to the literature with slight modifications.[1]

4-Aminopyridine (3.5 g, 37.2 mmol) was dissolved in a mixture of triethylamine (7.3 mL, 52.7 mmol) and THF (40 mL) and added dropwise to a solution of 1,3,5-benzene tricarboxytrichloride (3.3 g, 12.4 mmol) in THF at 0 °C under stirring. The reaction mixture was stirred for 8 h and allowed to warm up to room temperature. The crude product was filtered off, washed with THF (4x30 mL) and recrystallized from a mixture of H_2O (300 mL) and DMSO (140 mL). The pale yellowish precipitate was filtered off and washed with acetone (3×30 mL). The obtained product was dried under high vacuum (~ 5×10^{-2} mbar) at 30 °C overnight (4.0 g, 9.1 mmol, 73%).

Section 2 Analytics

Section 2.1 Nuclear magnetic resonance spectroscopy analysis

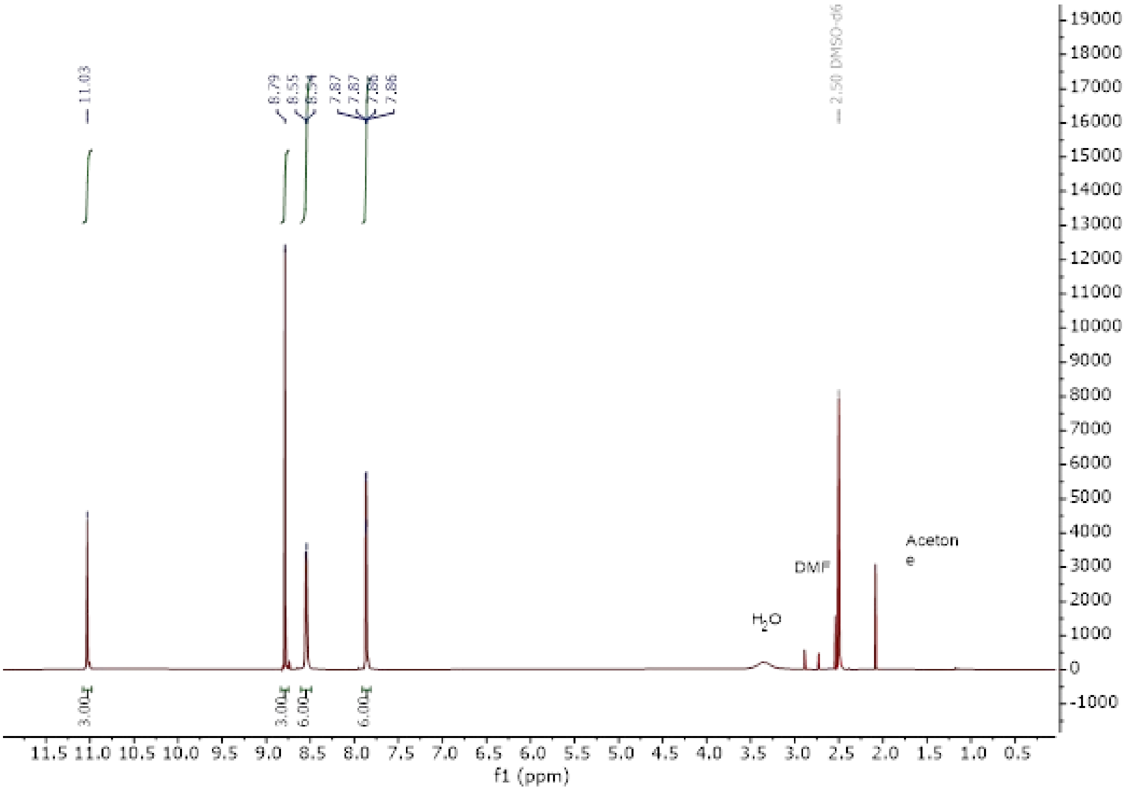

Fig. S1 NMR spectrum of N,N',N''-tris-(pyrid-4-yl)-trimesamide (TPAMA).
^{1}H NMR (DMSO-d_6, 300 MHz) δ: 11.03 (s, 3H), 8.79 (s, 3H), 8.55 (d, J = 5.6 Hz, 6H), 7.89-7.82 (m, 6H).

Section 2.2 Sample preparation for atomic absorption spectroscopy (AAS)

Analyte preparation method: a precisely weighted dried (*i.e.* degassed in vacuum until no guest molecules were present) sample of approx. 5 mg was suspended in *aqua regia* solution (3:1 conc. HCl and HNO_3 mixture) and the liquid was slowly boiled under stirring in a fume-hood until near complete evaporation of the liquid. The treatment by aqua regia solution was repeated two times, which yielded a clear solution prior to final evaporation. Finally, the obtained residue was dissolved in a fresh portion of diluted *aqua regia* (5 mL *aqua regia* + 10 mL ultra-pure water) and stirred overnight. The solution was filtered, the filter was carefully washed multiple times with ultra-pure water, and the filtrate was diluted precisely to 50 mL in a volumetric flask to yield the solution used for the determination of Ni and Fe content in the samples.

Section 2.3 Sample preparation for powder X-ray diffraction (PXRD) and additional information regarding the measurements

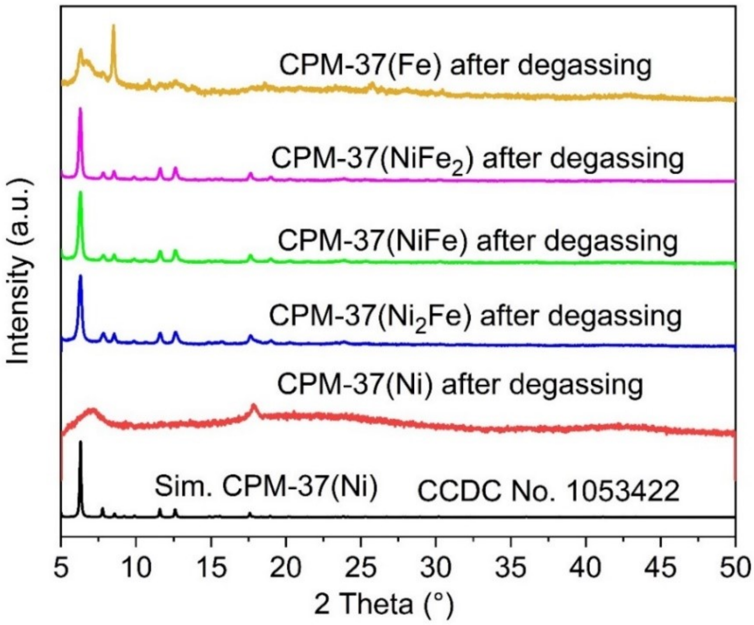

Fig. S2 PXRD patterns of the samples after the degassing in vacuum (5 10^{-2} Torr) at 60 °C for 16 h.

The CPM-37 samples were treated by CH_2Cl_2 in order to exchange the less-volatile guest molecules. For that ~30 mg of a sample was soaked in 30 mL CH_2Cl_2 for 5 days, while the CH_2Cl_2 was refreshed every day by accurate decantation and refilling the vial and degassing in vacuum (~5 10^{-2} Torr) at 60 °C for 16 h.

The PXRD of CPM-37(Ni) exhibited broad peaks, particularly well-recognizable around 6.4°, showing partial loss of crystallinity (note that the as-synthesized material consists of well-formed single crystals, whose identity were confirmed by single crystal structure determination, thereby demonstrating the excellent crystallinity). Similarly, the CPM-37(Fe) has also suffered partial loss of crystallinity. In contrary, all the bimetallic CPM-37(Ni,Fe) samples showed sharp PXRD peaks and high surface areas after degassing, indicating that the improved stability evidently stems from the presence of both iron and nickel, i.e. their synergism in the context of structural stability.

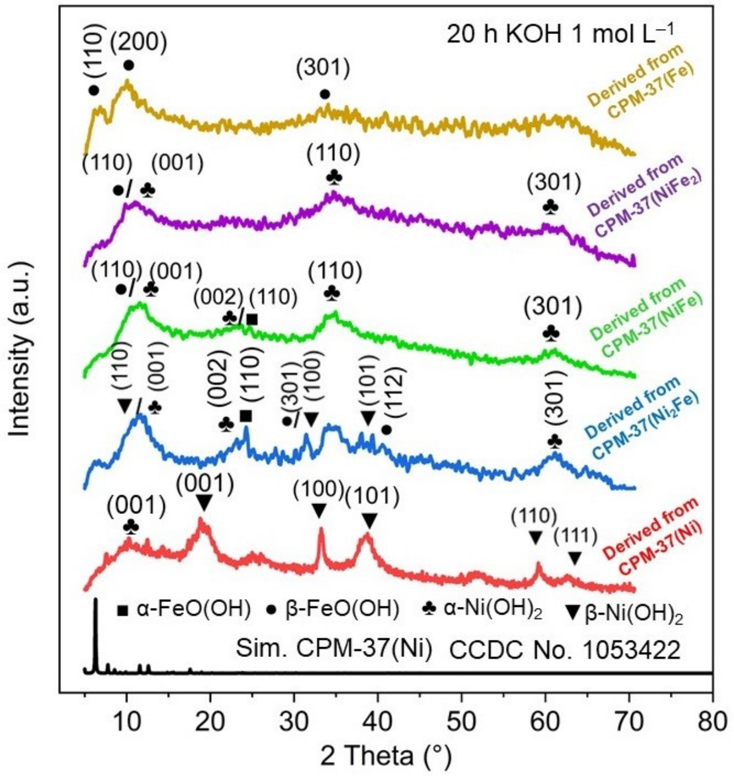

Fig. S3 PXRD patterns of the CPM-37(Ni), CPM-37(NiFe), CPM-37(Ni$_2$Fe) CPM-37(NiFe$_2$) and CPM-37(Fe) after 20 h in 1 mol L^{-1} KOH solution.

Section 2.4 Infrared spectroscopy (IR)

Fourier transform infrared spectroscopy (FT-IR) measurements were conducted by a Bruker TENSOR 37 IR spectrometer in the range of 4000–400 cm^{-1}. About 0.1 mg of the sample was mixed with dried KBr (the mass percentage of sample per KBr was about 1-2%) and grinded to fine powder. The resulted fine powder was pressed between two stainless steel disks to form a pellet, which was the actual subject of the measurement.

Table S1 FT-IR band assignment for as-synthesized CPM-37(Ni), CPM-37(Fe), and the bimetallic CPM-37(Ni,Fe) series (cm^{-1}).

Vibration	**CPM-37(Ni) (cm^{-1})**	**CPM-37(Ni$_2$Fe) (cm^{-1})**	**CPM-37(NiFe) (cm^{-1})**	**CPM-37(NiFe$_2$) (cm^{-1})**	**CPM-37(Fe) (cm^{-1})**
ѵ (OH)[2]	3434	3421	3401	3421	3434
ѵ ($C_{Ar}H$)[3]	2923	2962 2921	2970 2929	2962 2917	2929
ѵ (N–H)[4] (amide)	3085	3078	3083	3087	3074
v(C=O) (of the residual DMF) / δ(O–H)[5]	1664	1699	1691	1699	1695
ѵ$_{as}$ (OCO)[6]	1602 1506	1598 1513	1600 1512	1600 1515	1600 1613
ѵ$_{s}$(OCO) [7]	1384 1332	1394 1338	1402 1336	1392 1324	1398 1332
C–N amide[8]	1290	1292	1294	1292	1294
ѵ (C–N)(of DMF)[9]	1209	1296	1215	1216	1207
ѵ (C–N) (of DMF)/ѵ(C–C)$_{Ar}$[10] and	1101	1110	1112	1113	1107
ρ(C–H)$_{Ar}$, ɣ(C–H)$_{Ar}$[11]	1062 1020	….. 1027	1066 1027	…… 1020	….. 1014
δ(C–H)$_{Ar}$ /ѵ (C–C)$_{Ar\ 6}$	837 769	831 771	825 770	837 767	831 769
Ni–O, Fe–O[12]	536	538	536	537	537
Fe–O[13]	-	447	455	468	464

v = stretching vibration (vas= asymmetric, vs = symmetric vibration), δ = bending vibration (ρ = in plane, γ = out of plane vibration), Ar: the moiety belongs to an aryl group.

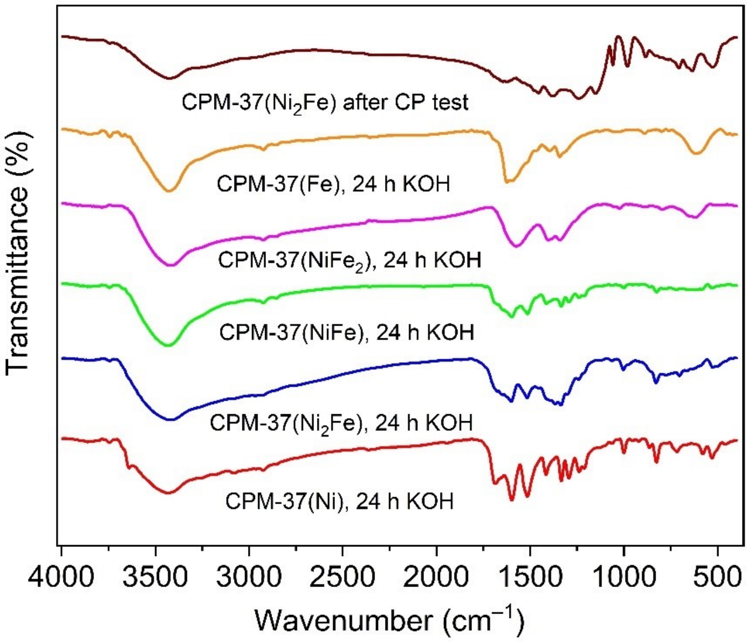

Fig. S4 FT-IR spectra of the CPM-37 after 20 h immersing in KOH 1 mol L^{-1}.

Table S2 Assignments of FT-IR-bands in the spectra of CPM-37(Ni), CPM-37(Fe), and the bimetallic CPM-37(Ni,Fe) series after treatment of the sample by 1 mol L^{-1} KOH aqueous solution during 20 h and after CP test for 20 h.

Allocation	**CPM-37(Ni) (cm^{-1})**	**CPM-37(Ni$_2$Fe) (cm^{-1})**	**CPM-37(NiFe) (cm^{-1})**	**CPM-37(NiFe$_2$) (cm^{-1})**	**CPM-37(Fe) (cm^{-1})**	**CPM-37(Ni$_2$Fe) (cm^{-1}) after CP test**
ν (OH)[2]	3433	3437	3438	3425	3431	3444
O–H bend layered in H_2O [14]	1600	1606	1601	1587	1618	----
O–H freely rotating water molecules [15]	1510 1330	1523 1361	1508 1379	---- 1378	---- 1379	---- 1363
Combination of lattice modes[15]	1000 827	1008 823	1012 828	1022 813	1043 877	1058 981
Translation modes of OH,[16] influenced by Fe^{3+}	----	----	----	611	597	634
ν(Ni–O)[17]	528	516	530	----	----	518

Section 2.5 Optical microscopy

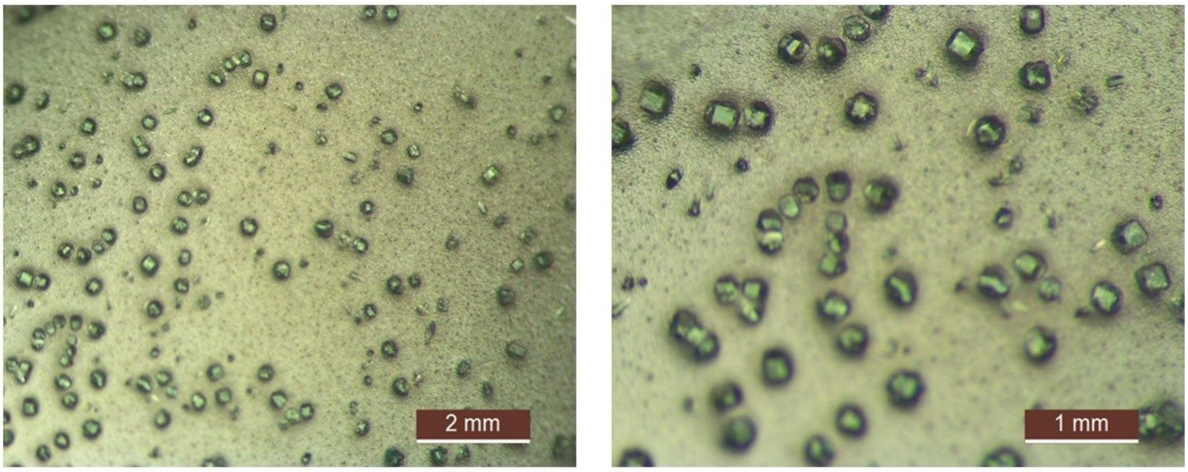

Fig. S5 Light microscopy images of the synthesized CPM-37(Ni) sample.

Section 2.6 Scanning electron microscopy (SEM) and energy dispersive X-ray analysis (EDX)

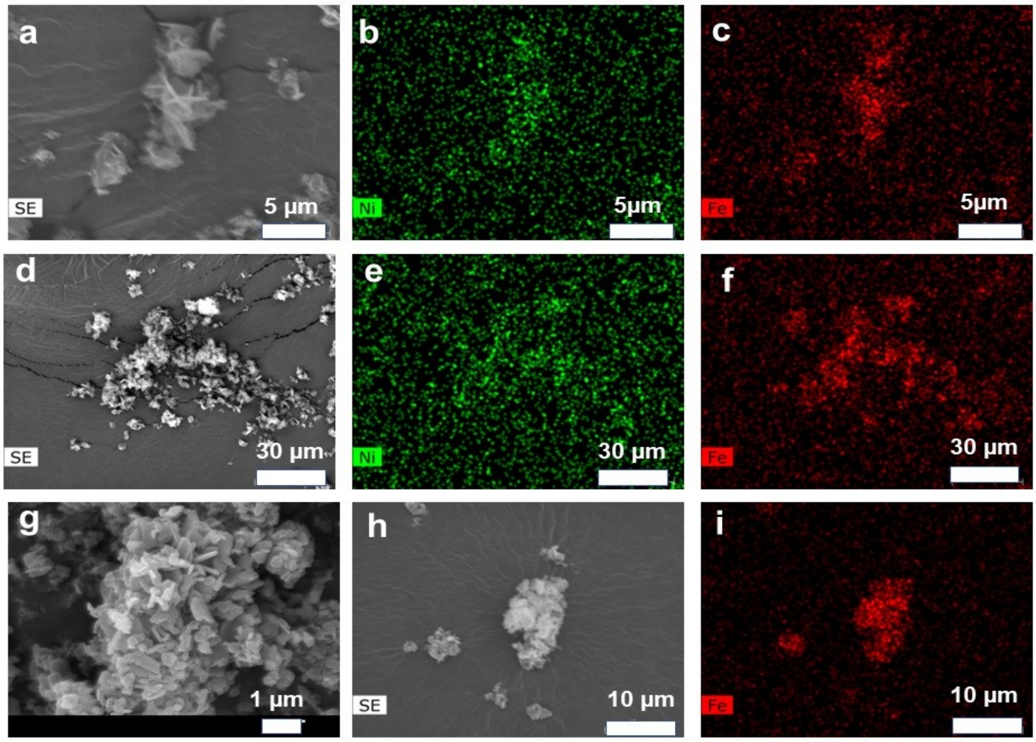

Fig. S6 SEM-EDX mapping images: (a-c) CPM-37(NiFe); (d-f) CPM-37(NiFe$_2$); (g-i) CPM-37(Fe).

Table S3 Raw SEM-EDX data for the CPM-37 samples [a)].

Element / **Sample**	**Fe**		**Ni**	
	Wt%(raw)	**At%(raw)**	**Wt%(raw)**	**At%(raw)**
CPM-37(Fe)	11.6	3.5	----	-----
CPM-37(Ni$_2$Fe)	7.7	2.5	12.7	4.0
CPM-37(NiFe)	8.8	2.9	8.8	2.8
CPM-37(NiFe$_2$)	12.2	3.9	5.5	1.7
CPM-37(Ni)	----	----	15.0	4.5

a) Values for C, O, N and Au, Cu which stem from the sample holder are not given, hence the given values do not add up to 100%.

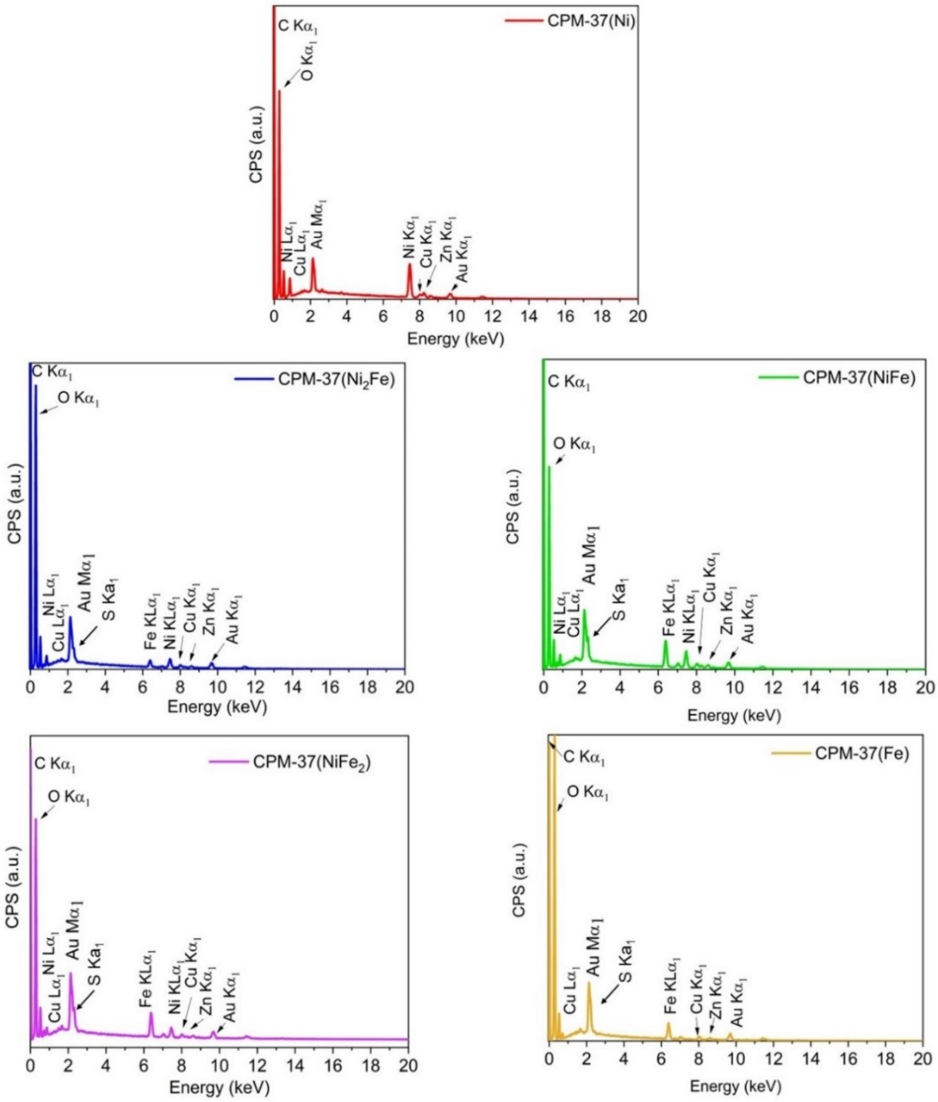

Fig. S7 SEM-EDX spectra of the CPM-37 samples.

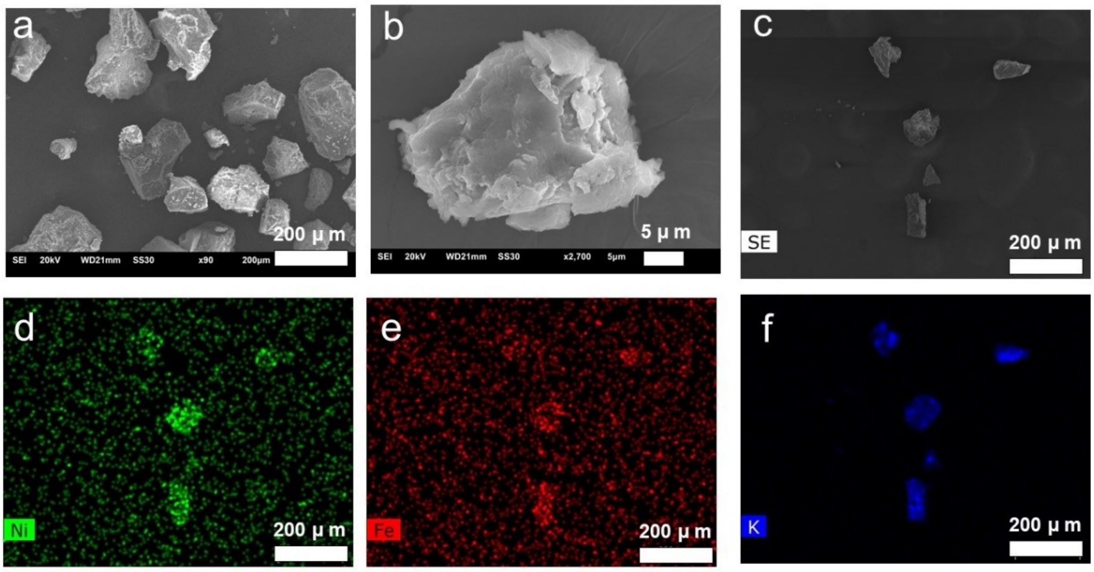

Fig. S8 SEM-EDX mapping of CPM-37(Ni_2Fe) after treatment of the sample by 1 mol L^{-1} KOH aqueous solution during 20 h.

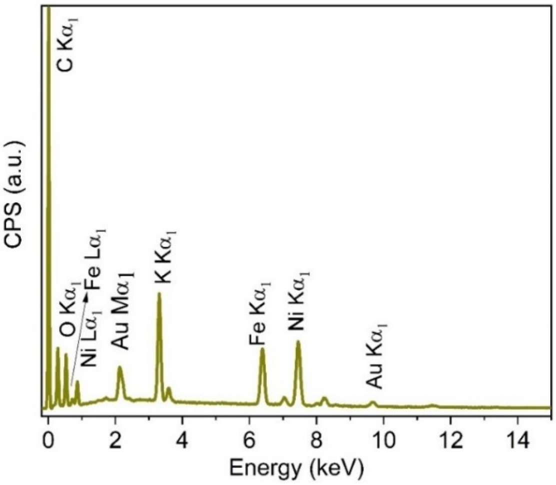

Fig. S9 SEM-EDX spectrum of CPM-37(Ni_2Fe) after treatment of the sample by 1 mol L^{-1} KOH aqueous solution during 20 h.

Table S4 SEM-EDX result of CPM-37(Ni_2Fe) soaking in 1 mol L^{-1} KOH aqueous solution for 20 h.

Element [a)]	Weight%(raw)	Atomic% (raw)	Relative ratio
Ni	5.4	4.7	2.04
Fe	2.5	2.3	1

[a)] Values for C, O, K, Au and Cu which stem from the sample holder are not given, hence the given values do not add up to 100%.

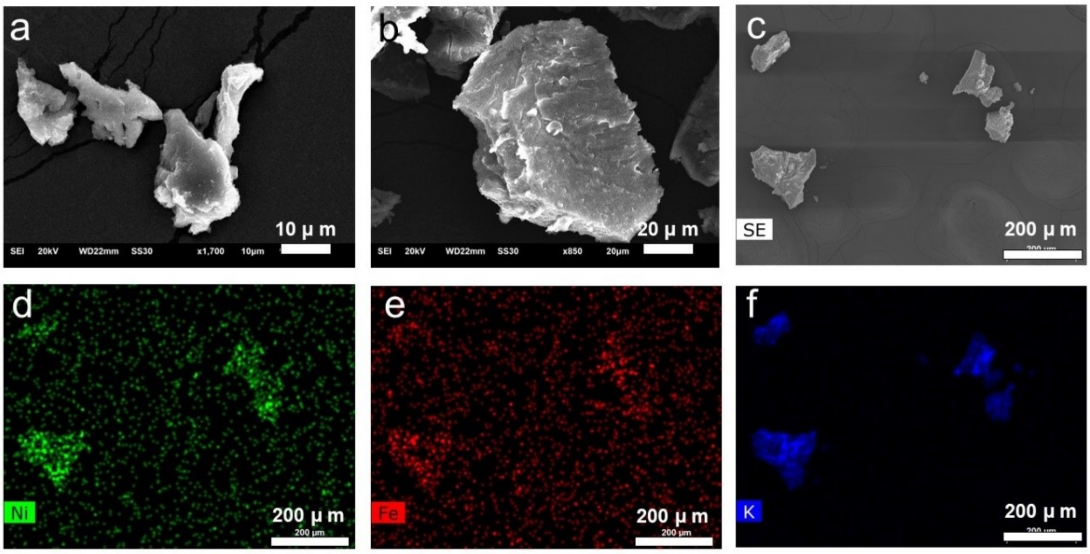

Fig. S10 SEM-EDX mapping of CPM-37(Ni_2Fe) after chronopotentiometry analysis (CP) in 1 mol L^{-1} KOH aqueous solution for 20 h.

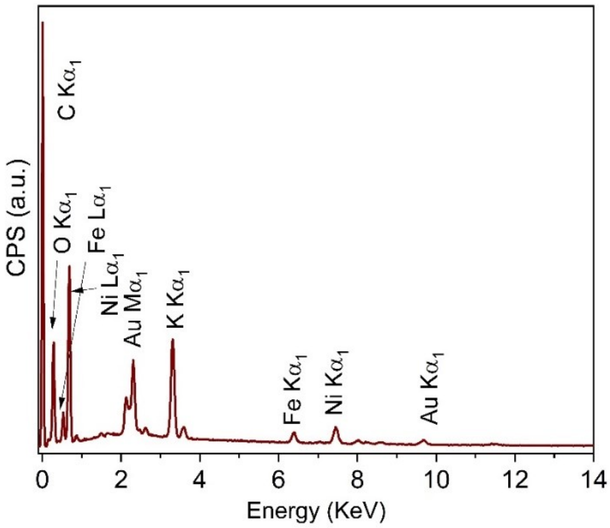

Fig. S11 SEM-EDX spectrum of CPM-37(Ni_2Fe) after CP in 1 mol L^{-1} KOH aqueous solution for 20 h.

Table S5 SEM-EDX result of CPM-37(Ni_2Fe) after CP in 1 mol L^{-1} KOH aqueous solution for 20 h.

Element [a)]	**Weight% (raw)**	**Atomic% (raw)**	**Relative ratio**
Ni	15.5	15.1	1.7
Fe	6.7	8.9	1

[a)] Values for C, O, Au, K and Cu which stem from the sample holder are not given, hence the values do not add up to 100%.

Section 2.7 Thermogravimetry analysis (TGA)

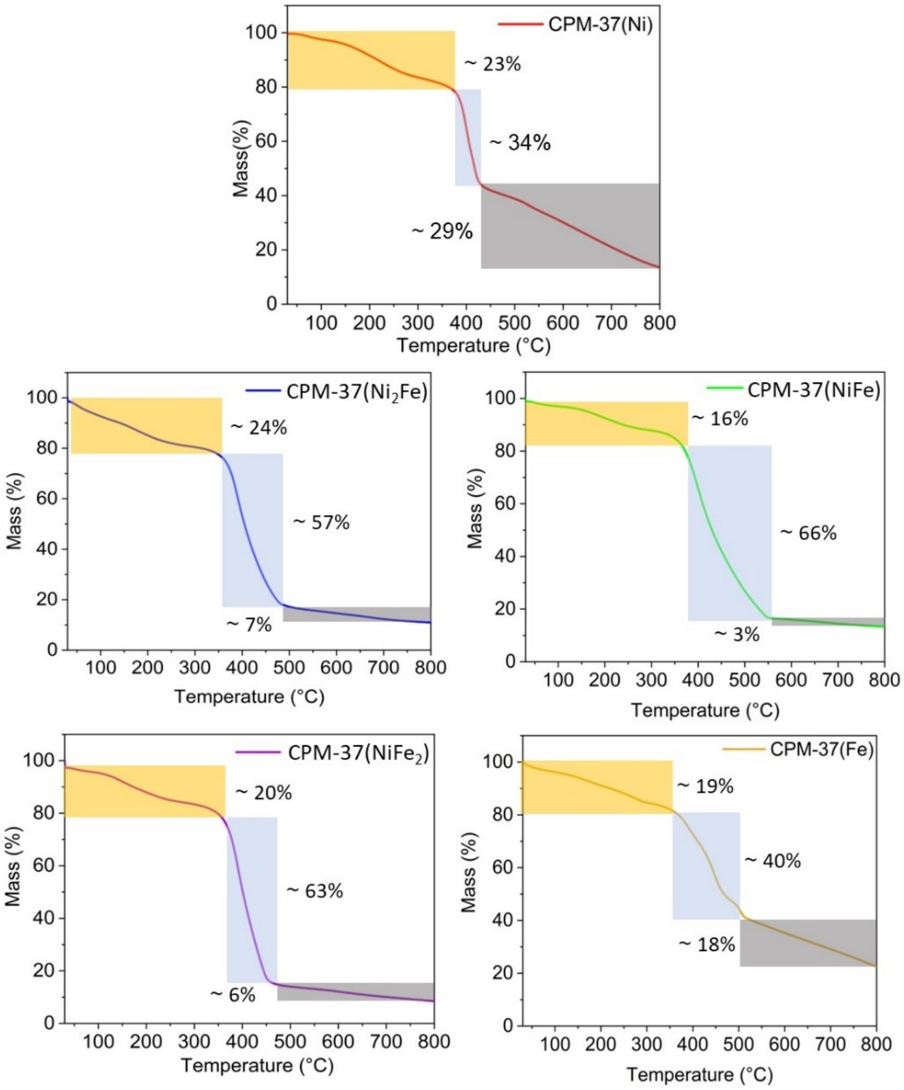

Fig. S12 TGA curves for CPM-37(Ni), CPM-37(Ni_2Fe), CPM-37(NiFe), CPM-37($NiFe_2$), and CPM-37(Fe) samples. The measurements were done using N_2 as a carrier gas with a heating rate of 5 K min^{-1}.

Section 2.8 X-ray photoelectron spectroscopy (XPS)

Section 2.8.1 X-ray photoelectron spectroscopy (XPS) of CPM-37(Ni), CPM-37(Fe), and CPM-37(Ni_2Fe)

The XPS spectra of CPM-37(Ni), CPM-37(Fe), and CPM-37(Ni_2Fe) are presented in Fig. S13a, confirming the presence of Ni, C, O, and N in CPM-37(Ni); Fe, C, O, and N in CPM-37(Fe); and Ni, Fe, C, O, and N in CPM-37(Ni_2Fe). The high-resolution XPS spectrum of C1s for all samples was subjected to deconvolution, resulting in four distinct peaks attributed to (C–C, C–H), (C–N), (C–O–C, C–OH), and (O–C=O) bands.[18] The position of each peak is assigned in Table S8. The high-resolution spectrum of O1s can be deconvoluted into three main peaks corresponding to M–O, O=C–O, and O–H functionalities.[19,20] The positions of these peaks are provided in Table S9. Moreover, N 1s in the samples can be deconvoluted to two peaks (amidic N) and (pyridinic N) [21] Fig. S13 d. It should be considered that the pyridinic nitrogen are located almost at the same binding energy (399.5) independently on whether it is coordinated or not. The binding energy peaks of N1s are listed in Table S9.

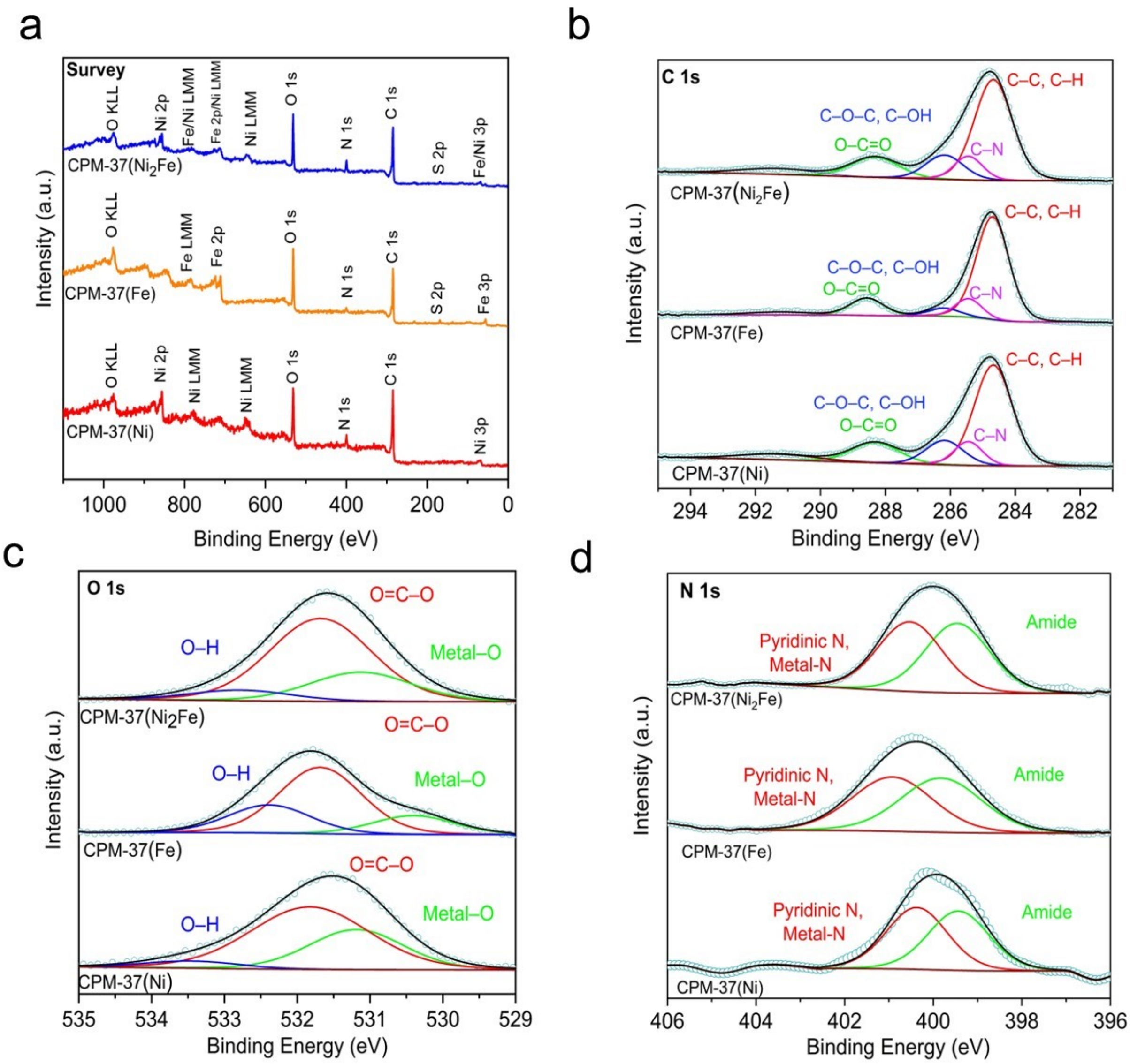

Fig. S13 XPS survey and high-resolution spectra of CPM-37(Ni), CPM-37(Fe) and CPM-37($\mathrm{Ni_2Fe}$).(a) Survey spectra of CPM-37(Ni), CPM-37(Fe) and CPM-37($\mathrm{Ni_2Fe}$); (b) C 1s high-resolution spectra of CPM-37(Fe) and CPM-37($\mathrm{Ni_2Fe}$); (c) O 1s high-resolution spectra of CPM-37(Fe) and CPM-37($\mathrm{Ni_2Fe}$); (d) N 1s high-resolution spectra of CPM-37(Fe) and CPM-37($\mathrm{Ni_2Fe}$).

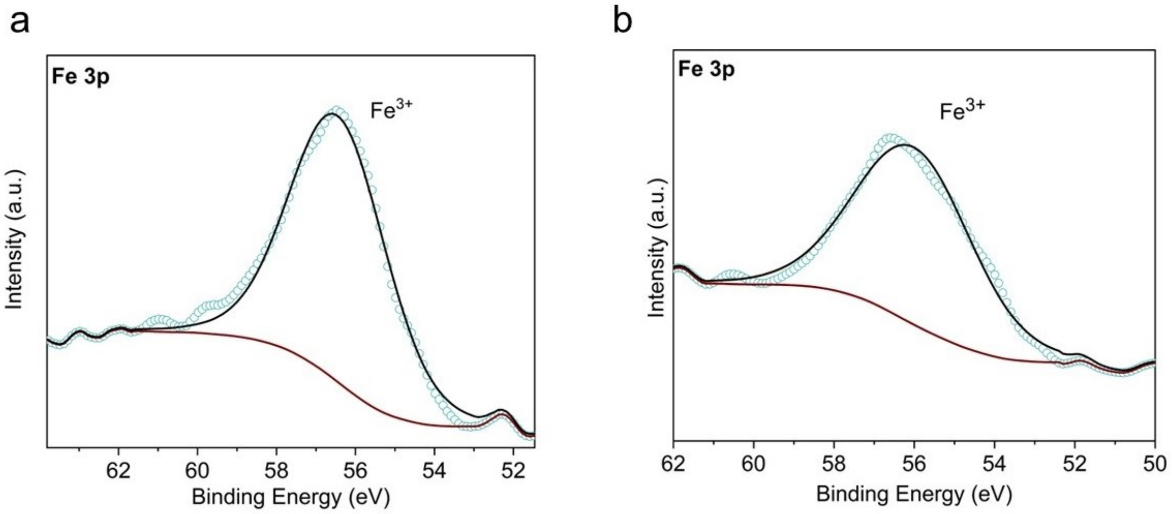

Fig. S14 High-resolution spectrum of Fe 3p: a) CPM-37(Fe), b) CPM-37(Ni_2Fe).

Fig. S14 illustrates the deconvolution of the high-resolution spectrum of Fe 3p, revealing main peaks at 56.4 and 56.3 eV for CPM-37(Fe) and CPM-37(Ni_2Fe), respectively. These results confirm the presence of Fe^{3+} as the predominant oxidation state of Fe in both CPM-37(Fe) and CPM-37(Ni_2Fe).[22]

Table S6 XPS quantitative elemental analysis of CPM-37(Ni), CPM-37(Fe), and CPM-37(Ni_2Fe).

Catalyst	Ni (At%)	Fe (At%)	O (At%)	N (At%)	S (At%)	C (At%)
CPM-37(Ni)	3.76	-----	18.27	5.65	-----	72.32
CPM-37(Fe)	-----	4.01	17.34	8.15	2.27	68.23
CPM-37(Ni_2Fe)	3.11	1.74	16.08	6.82	1.25	71.00

Table S7 XPS peak types and corresponding binding energies of carbon in CPM-37(Ni), CPM-37(Fe) and CPM-37(Ni_2Fe).

Element	Characteristic peak	Catalyst	C–C,C–H (eV)	C–N (eV)	C–O–C, C–OH (eV)	O–C=O (eV)
C	C 1s	CPM-37(Ni)	284.7	285.4	286.2	288.5
		CPM-37(Fe)	284.7	285.5	286.2	288.6
		CPM-37(Ni_2Fe)	284.7	285.5	286.2	288.5

Table S8 XPS peak types and corresponding binding energies of oxygen in CPM-37(Ni), CPM-37(Fe) and CPM-37(Ni_2Fe).

Element	Characteristic peak	Catalyst	Metal–O (eV)	O=C–O (eV)	O–H (eV)
O	O 1s	CPM-37(Ni)	531.1	531.8	533.2
		CPM-37(Fe)	530.4	531.7	532.4
		CPM-37(Ni_2Fe)	531.2	531.7	532.8

Table S9 XPS peak types and corresponding binding energies of nitrogen in CPM-37(Ni), CPM-37(Fe) and CPM-37(Ni_2Fe).

Element	Characteristic peak	Catalyst (eV)	N_{amide} (eV)	$N_{Pyridine}$–Metal (eV)
N	N1s	CPM-37(Ni)	399.4	400.3
		CPM-37(Fe)	399.8	400.9
		CPM-37(Ni_2Fe)	399.5	400.6

Table S 10 XPS-based metal ratios and the ratios between different oxidation states of nickel and iron in CPM-37(Ni), CPM-37(Fe) and CPM-37(Ni_2Fe).

Sample		At% [a)]	Ni/Fe		At% [b)]	Position (eV)	M^{2+}/M^{3+}
CPM-37(Ni)	Ni	3.76	-----	Ni^{3+}	4.6	857.5	4.9
				Ni^{2+}	22.4	856.0	
	Fe	-----		Fe^{3+}	-----	-----	----
				Fe^{2+}	-----	-----	
CPM-37(Fe)	Ni	----	-----	Ni^{3+}	-----	-----	----
				Ni^{2+}	-----	-----	
	Fe	4.01		Fe^{3+}	36.3	711.6	----
				Fe^{2+}	-----	-----	
CPM-37(Ni_2Fe)	Ni	3.11	1.8	Ni^{3+}	10.1	857.1	2.4
				Ni^{2+}	24.0	855.9	
	Fe	1.74		Fe^{3+}	43.8	711.9	----
				Fe^{2+}	-----	-----	

a) From XPS survey spectrum, b) Based on the Ni $2p_{3/2}$ and Fe $2p_{3/2}$ regions in XPS, At% Ni $2p_{1/2}$ and the satellites are not given, hence the values do not add up to 100%.

Section 2.8.2 X-ray photoelectron spectroscopy (XPS) of 37(Ni2Fe) after OER

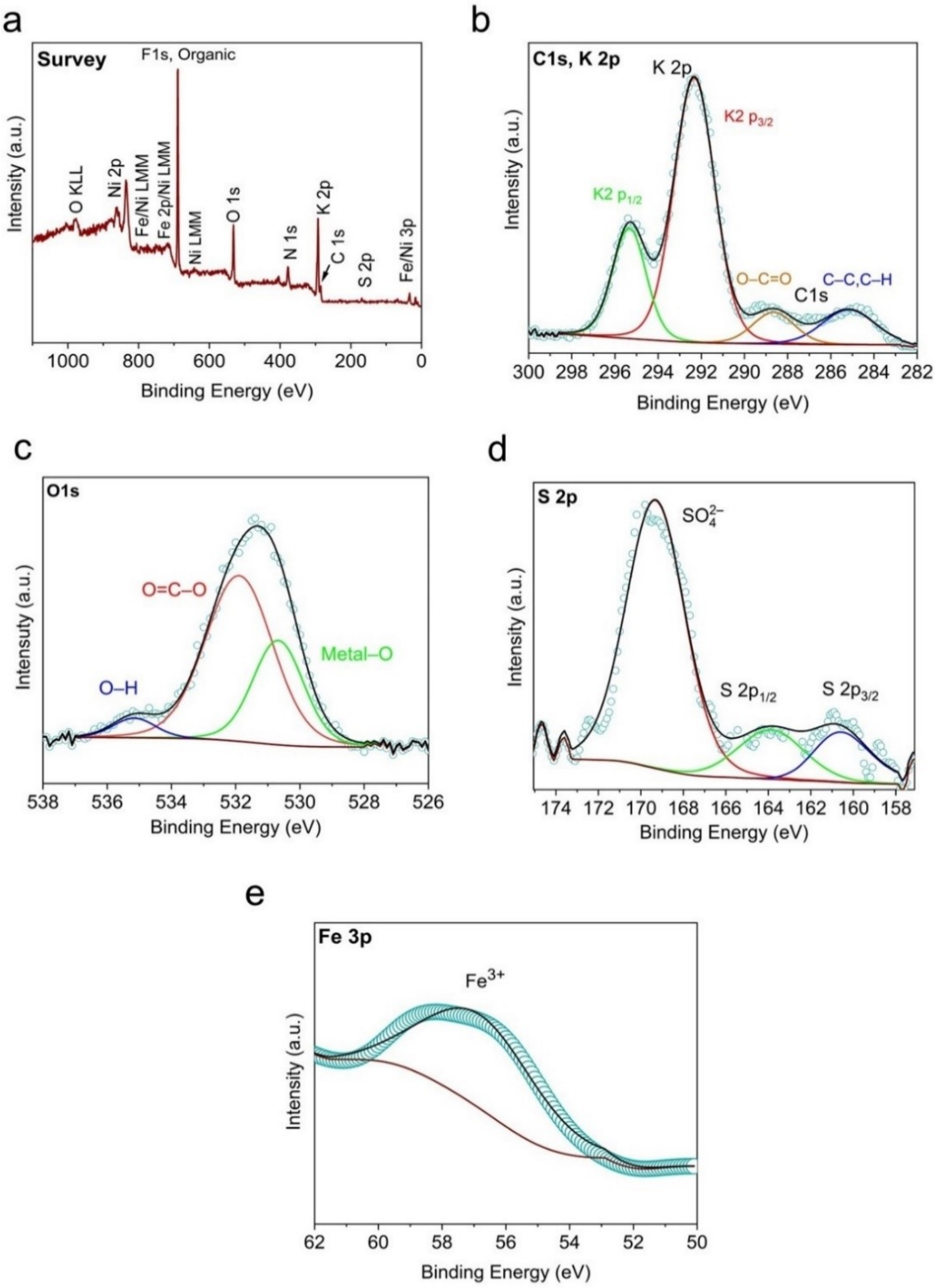

Fig. S15 XPS survey and high-resolution spectra of CPM-37(Ni_2Fe) after CP in 1 mol L^{-1} for 20 h.(a) Survey spectra of CPM-37(Ni_2Fe) CPM-37(Ni_2Fe) after CP in 1 mol L^{-1} for 20 h ; (b) C 1s and K 2p high-resolution spectra of CPM-37(Ni_2Fe) after CP in 1 mol L^{-1} for 20 h; (c) O 1s high-resolution spectra of CPM-37(Ni_2Fe) after CP in 1 mol L^{-1} for 20 h; (d) S 2p high-resolution spectra of CPM-37(Ni_2Fe) after CP in 1 mol L^{-1} for 20 h.

The XPS spectra of derived electrode materials from CPM-37(Ni_2Fe) after the CP test are presented in Fig. S15a, confirming the presence of and Ni, Fe, C, O, N, K, and F in CPM-

37(Ni_2Fe). Note that the presence of potassium is due to the treatment by the 1 mol L^{-1} KOH alkaline solution, while the fluorine is present in the residues of polyvinylidene fluoride (PVDF), which is used as a binder to for the electrode coating. Fig. S15b presents the high-resolution spectrum of K 2p (K $2p_{1/2}$ at 295.3 eV and K $2p_{2/3}$ at 292.3 eV), along with C1s (C–C, C–H at 284.9 eV, associated with the binder) and (O–C=O at 288.5 eV, associated with adventitious carbon, e.g. in the form of metal (hydroxo)carbonates forming due to anodic oxidation of carbon containing species).[23] The high-resolution spectrum of O1s can be deconvoluted into three main peaks which are assumed to be corresponding to M–O (531.8 eV), O=C–O (532.5 eV) and O–H (535.5 eV) (originating from adventitious carbon or residual organic linkers.[19] Fig. 15d exhibits a sharp peak located at 169.4 eV, which can be attributed to the sulfate groups originating from $FeSO_4 \cdot 7H_2O$. Additionally, two smaller peaks at 163.7 and 160.5 correspond to S $2p_{1/2}$ and S$2p_{3/2}$, respectively.[24] Deconvolution of the high-resolution spectrum of Fe 3p revealed main peaks at 57.3 eV, confirming the presence of Fe^{3+} as the predominant oxidation state of Fe in the derived electrode materials from CPM-37(Ni_2Fe) after the OER.

Table S11 The metal ratios and the ratios between different oxidation states of derived electrode materials from CPM-37(Ni_2Fe) after CP test.

Sample		**At% a)**	**Ni/Fe**		**At% b)**	**Position (eV)**	**M^{2+}/M^{3+}**
Derived electrode materials from CPM-37(Ni_2Fe) after the CP test	Ni	2.61	1.8	Ni^{3+} c)	10	858.7	2.4
				Ni^{2+} d)	24	855.7	
	Fe	1.46		Fe^{3+}	42.6	709.9 e) 711.2 712.7 713.9	----
				Fe^{2+}	-----		

a) From XPS survey spectrum, b) Based on the Ni $2p_{3/2}$ and Fe $2p_{3/2}$ regions in XPS. b) derived from NiO(OH) d) derived from $Ni(OH)_2$, e) Gupta and Sen (GS) multiplets fitting method.

Section 2.9 CPM-37($Ni_{2.5}Fe_{0.5}$) and CPM-37($Ni_{0.5}Fe_{2.5}$) additional representatives: a further step towards understanding the stability of CPM-37(Ni,Fe) materials.

The comparison of the activated 'primary series' mixed-metal CPM-37(Ni,Fe) as well as the single-metal CPM-37(Fe) and the known CPM-37(Ni) shows that the mixed-metal materials possess much higher stability, while the single-metal materials demonstrate no permanent porosity. As all the found surface areas for the mixed-metal CPM-37s are close, it is interesting, at which composition the deterioration sets-in. In order to test those conditions, we have synthesized two additional CPM-37($Ni_{0.5}Fe_{2.5}$) and CPM-37($Ni_{2.5}Fe_{0.5}$) representatives with higher metal ratios according to the standard method (the Ni:Fe ratio corresponds to the initial ratio of reagents). The syntheses were performed in parallel, together with the re-synthesis of a batch of CPM-37(Ni_2Fe) to check the reproducibility and establishing the comparability of the results though the latter "benchmark" (for the latter only the surface area determination and the TGA were performed).

The new materials were analyzed using PXRD, SEM-EDX, TGA, and N_2 gas adsorption to improve the understanding of the structure-stability trends. These newly synthesized compounds are given separately from the others, as not a full set of analyses were done, but only the most relevant and accessible ones in the context of stability.

Synthesis. The syntheses of the new representatives, CPM-37($Ni_{0.5}Fe_{2.5}$) and CPM-37($Ni_{2.5}Fe_{0.5}$), were performed precisely according to the method, described for CPM-37(Ni) in the main part of the paper. The quantities of the reactants/solvent used are given below:

Synthesis of CPM-37($Ni_{2.5}Fe_{0.5}$)

The synthesis was performed according to the general method using 0.125 mmol (36.35 mg) of $Ni(NO_3)_2\cdot 6H_2O$, 0.025 mmol (6.95 mg) of $FeSO_4\cdot 7H_2O$ 0.15 mmol (36.33 mg) of H_2BPDCA, 0.05 mmol (21.92 mg) and 12 mL of DMF in a thick wall 20 mL crew cap glass vial. Yield: 63 mg.

Synthesis of CPM-37($Ni_{0.5}Fe_{2.5}$)

The synthesis was performed according to the general method using 0.025 mmol (7.27 mg) of $Ni(NO_3)_2\cdot 6H_2O$, 0.125 mmol (34.75 mg) of $FeSO_4\cdot 7H_2O$, 0.15 mmol (36.33 mg) of H_2BPDCA, 0.05 mmol (21.92 mg) of TPAMA, and 12 mL of DMF. Yield: 59 mg.

PXRD. The PXRD patterns of the as-synthesized CPM-37($Ni_{2.5}Fe_{0.5}$) and CPM-37($Ni_{0.5}Fe_{2.5}$) confirmed the successful synthesis (Fig. S16; compare with Fig. 2 with the 'primary series'). The as-synthesized compound CPM-37($Ni_{2.5}Fe_{0.5}$) has somewhat inferior crystal quality, compared to other mixed-metal CPM-37s, while the CPM-37($Ni_{0.5}Fe_{2.5}$) has a high quality. An interesting peculiarity worth mentioning is that the peak at ~8° appears to be particularly intense for CPM-37($Ni_{0.5}Fe_{2.5}$), which is similar to CPM-37(Fe), compared to all other CPM-37s. The reason is a preferred orientation as both samples consist of more distinct hexagonal plates than the other synthesized CPM-37s (see Fig. S6 and S17 for the respective SEM images).

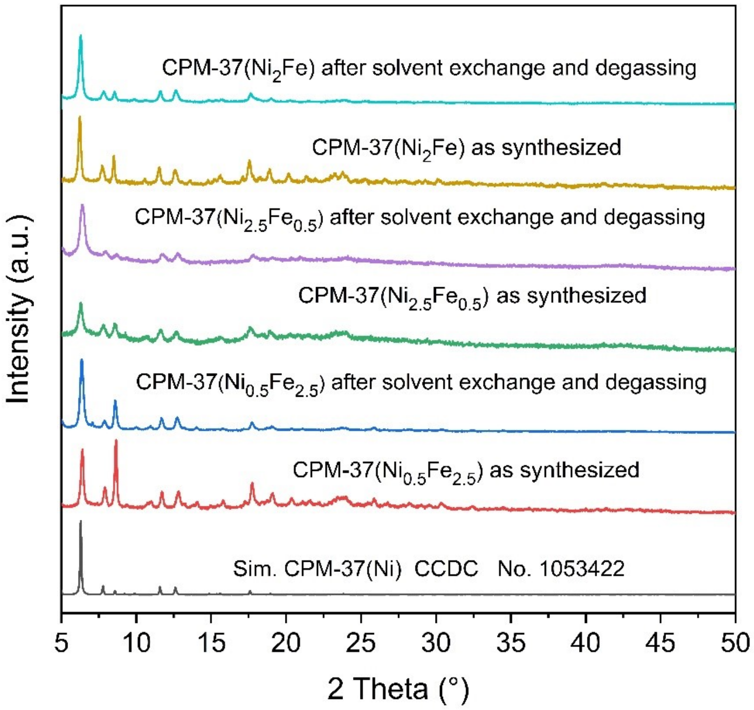

Fig. S16 PXRD patterns of the additional CPM-37($Ni_{2.5}Fe_{0.5}$) and CPM-37($Ni_{0.5}Fe_{2.5}$) compared to CPM-37(Ni_2Fe) (all in 'as synthesized' and 'after solvent exchange and degassing' forms).

The PXRDs of the solvent exchanged and degassed CPM-37($Ni_{2.5}Fe_{0.5}$) and CPM-37($Ni_{0.5}Fe_{2.5}$) demonstrate the general retention of the crystallinity and the high similarity to the other CPM-37s. The sample preparation was strictly identical to the one used for the 'primary series': the solvent exchange with CH_2Cl_2 for three days was followed by degassing at 80°C for 15 hours). Notably, the supposed effect of the preferred orientation for CPM-37($Ni_{0.5}Fe_{2.5}$) weakens, probably due to small relative movements of the crystals during the degassing. The retention of the crystallinity compared to the single-metal CPM-37(Ni) and CPM-37(Fe) corroborates to the stabilizing role of even a relatively small addition of the second metal in the context of permanent porosity.

SEM. Scanning electron microscopy (SEM) images of the samples are given in Fig. S17 (compare with Fig. S6 for the other samples and note the more distinct larger hexagonal platelets for CPM-37($Ni_{0.5}Fe_{2.5}$) and CPM-37(Fe), which is the likely reason for the preferred orientation effects in the PXRD, discussed above). The EDX mapping demonstrates the uniform distribution of nickel and iron in the samples, supporting their expected homogeneity.

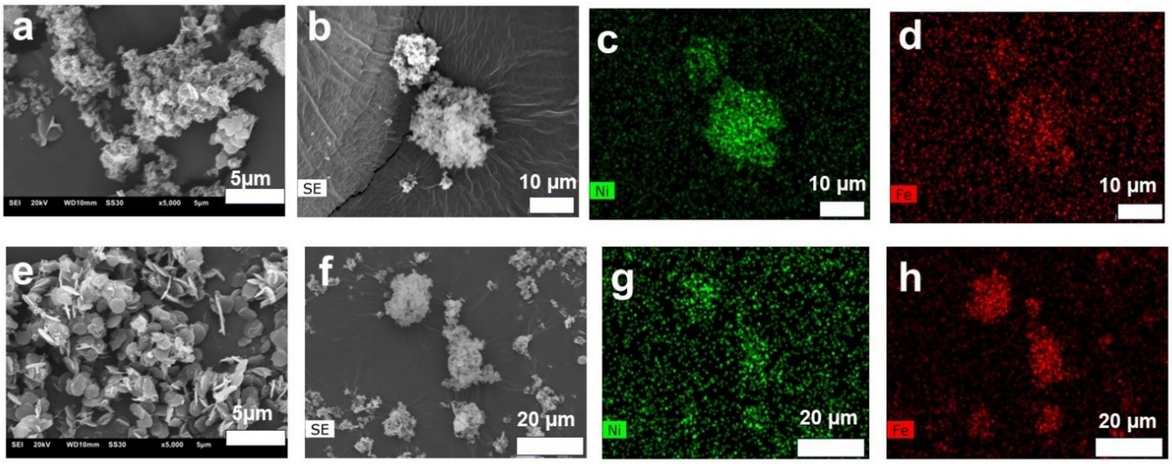

Fig. S17 a) SEM images and b-d) SEM-EDX mapping of CPM-37($Ni_{2.5}Fe_{0.5}$). e) SEM images and f-h) SEM-EDX mapping of CPM-37($Ni_{0.5}Fe_{2.5}$).

Table S12 Ni and Fe content in the additionally synthesized CPM-37($Ni_{2.5}Fe_{0.5}$) and CPM-37($Ni_{0.5}Fe_{2.5}$) materials according to SEM-EDX.

Sample	**SEM-EDX**	**Expected, reactant-based**
	Found Ni/Fe mol. ratio	Initial Ni/Fe mol. ratio
CPM-37($Ni_{2.5}Fe_{0.5}$)	3.93	5.00
CPM-37($Ni_{0.5}Fe_{2.5}$)	0.21	0.20

The EDX-based element content of iron and nickel is summarized in Table S12 (compare with Table 1 for the ‘primary series’). While the EDX-based data is considered less accurate than AAS-based data, it showed sufficiently good correlation to the other samples and was used in the case of the additional materials for simplicity. Notably, CPM-37($Ni_{0.5}Fe_{2.5}$) had practically the same Ni:Fe content in the product as in the reaction medium (*i.e.* reactant-based), but CPM-37($Ni_{2.5}Fe_{0.5}$) showed a significant enrichment with iron, which could be interpreted as a tendency towards a more even metal composition (which is the most stable one near this composition range according to the proposed model).**TGA.** Thermogravimetric analysis (TGA) was conducted under N_2 after the solvent exchange and degassing for CPM-37($Ni_{0.5}Fe_{2.5}$), CPM-37($Ni_{2.5}Fe_{0.5}$), and for the resynthesized CPM-37(Ni_2Fe) (Fig. S18).

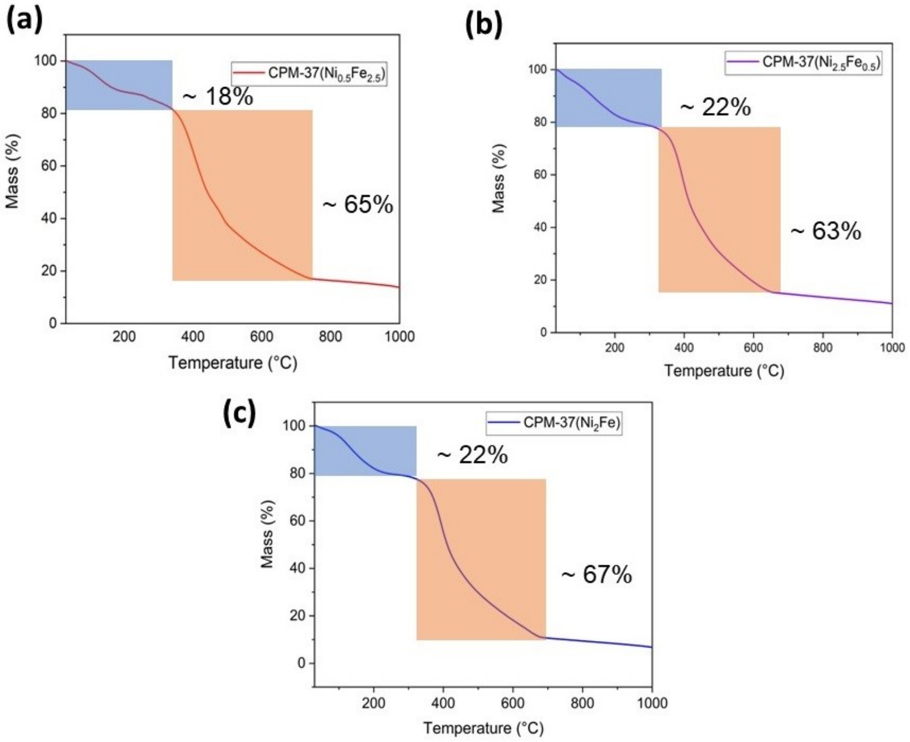

Fig. S18 TGA curves for a) CPM-37($Ni_{0.5}Fe_{2.5}$), b) CPM-37($Ni_{2.5}Fe_{0.5}$), c) CPM-37(Ni_2Fe). The measurements were done under N_2 with a heating rate of 2 K min^{-1}.

A specially introduced difference was the decreased heating rate at 2 K min^{-1} compared to the 5 K min^{-1} for the primary CPM-37s, which was done for checking the possibility of improving the precision. Normally, for MOF compounds, which are characterized with lesser crystallinity and uniformity compared to dense non-porous highly crystalline compounds, a decrease of heating rates gives no advantage (the TGA curve features are less well defined to begin with, due to irregularities). However, we wanted to check the possible effect of a slower heating rate by comparing the data for the resynthesized 'benchmark' CPM-37(Ni_2Fe) and to analyze whether additional fine features or better 'defined' TGA curves for CPM-37($Ni_{0.5}Fe_{2.5}$), CPM-37($Ni_{2.5}Fe_{0.5}$) could be observed.

The newly synthesized CPM-37($Ni_{0.5}Fe_{2.5}$) and CPM-37($Ni_{2.5}Fe_{0.5}$) feature similar TGA curves compared to the other CPM-37s, and the use of 2 K min^{-1} heating rate brings no visible improvements compared to 5 K min^{-1} (the resynthesized CPM-37(Ni_2Fe) is almost identical to the primary sample given in Fig. S12). TGA once more confirms that the removal of the DMF after solvent exchange and degassing is not complete, which potentially suggests that even higher surface areas are attainable. However, our attempt to significantly increase the degassing temperature led to decrease of the observed surface area, probably due to further loss of crystallinity. The published approach is the best compromise between guest solvent removal and stability which we were able to find.

N_2 adsorption. The data from N_2 adsorption for the degassed CPM-37($Ni_{0.5}Fe_{2.5}$) and CPM-37($Ni_{2.5}Fe_{0.5}$) are summarized in Fig. S19 and Table S13 (compare with the data for the primary CPM-37s in Fig. 4 and Table 2).

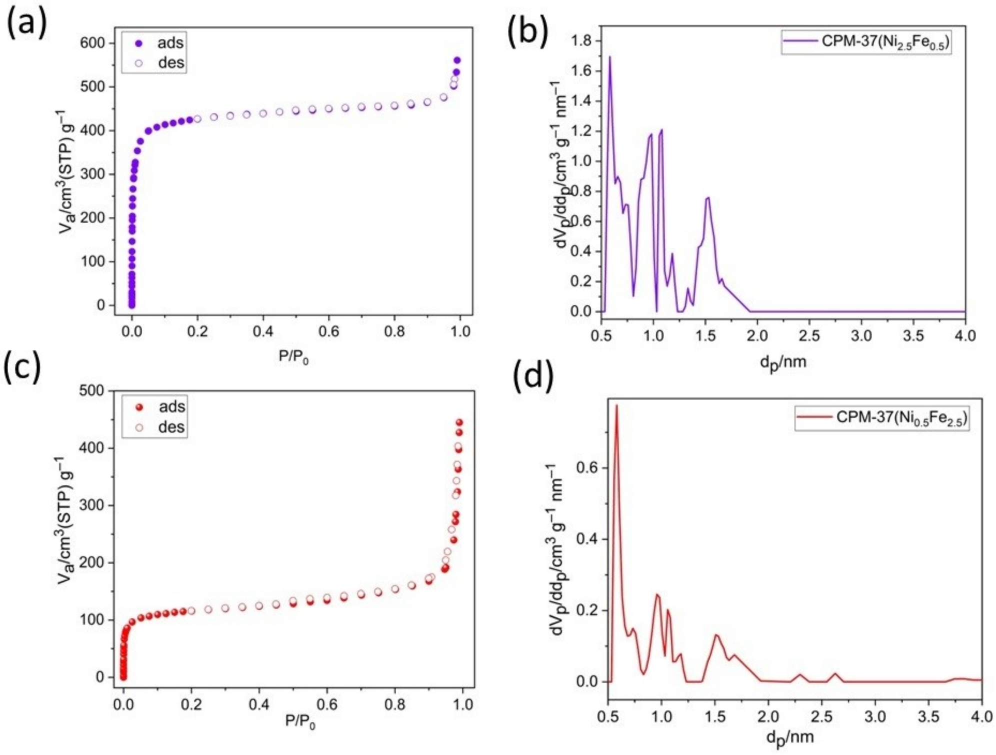

Fig. S19 (a,b) Nitrogen adsorption isotherm and pore size distribution of CPM-37($Ni_{2.5}Fe_{0.5}$). (c,d) Nitrogen adsorption isotherm and pore size distribution of CPM-37($Ni_{0.5}Fe_{2.5}$). Isotherms measured at 77 K (adsorption: filled circles; desorption: empty circles), NLDFT-based pore size distributions.

Table S13 N_2 adsorption results, BET surface area and total pore volume for the additionally synthesized CPM-37($Ni_{0.5}Fe_{2.5}$) and CPM-37($Ni_{2.5}Fe_{0.5}$).

Sample	BET surface area (m^2 g^{-1})	Total pore volume (cm^3 g^{-1}) [a)]
CPM-37($Ni_{2.5}Fe_{0.5}$)	1684	0.85
CPM-37($Ni_{0.5}Fe_{2.5}$)	435	0.68

[a)] The total pore volumes were determined at $p/p_0 = 0.90$ of the adsorption branches.

CPM-37($Ni_{2.5}Fe_{0.5}$) exhibits a high surface area of 1685 m^2 g^{-1}, which is just somewhat lower than the other mixed-metal MOFs of the ‘primary series’ (Ni:Fe ratio of ~2:1, 1:1, 1:2) with surface areas in the range of 1955-2378 $m^2\ g^{-1}$ (Table 2), and differs strongly from CPM-37(Ni) with 87 $m^2\ g^{-1}$. On the other hand, CPM-37($Ni_{0.5}Fe_{2.5}$) features a much lower surface area of 435 $m^2\ g^{-1}$ compared to other mixed-metal CPM-37s which is close to CPM-37(Fe) with 368 $m^2\ g^{-1}$.

In conclusion, the attempt to decrease the Fe content further in the CPM-37($Ni_{2.5}Fe_{0.5}$) compared to CPM-37(Ni_2Fe) led only to a slight decrease of stability in the context of permanent porosity. There are two plausible reasons for that: firstly, the actual Ni:Fe ratio in CPM-37($Ni_{2.5}Fe_{0.5}$) is closer to 4:1 than to the intented 5:1 (corresponding to the reactant ratio), *i.e.,* there is a tendency to iron enrichment, which would provide more Fe^{3+} for charge compensation and, supposedly, for a more stable formula. Secondly, even the single-metal CPM-37(Ni) demonstrate the presence of some Ni^{3+} according to the XPS data, and CPM-37(Ni_2Fe) had a Ni^{2+}:Ni^{3+} = 2.4 ratio so the amount of Fe^{3+} necessary for stabilization should be lower than assumed for the $Ni^{II}_2Fe^{III}$ composition. Thus, even CPM-37($Ni_{2.5}Fe_{0.5}$) with sufficient Ni^{3+} can mark the beginning of the range of supposedly stable compositions.

On the other hand, CPM-37($Ni_{0.5}Fe_{2.5}$) demonstrates a low surface area, close to CPM-37(Fe). In this case no tendency for Ni enrichment is registered and the Ni:Fe ratio is close to the metal ratio used for the synthesis. This is not surprising, as the $\{M_3O(RCOO)_6\}$ cluster should rather favor M^{3+} ions, even if the stability of the cationic framework is somewhat compromised in the absence of a M^{2+} constituent. Thus, a small amount of Ni^{2+} is not enough to stabilize the CPM-37($Ni_{0.5}Fe_{2.5}$) regarding permanent porosity.

In general, the results conform to the supposed model, even if there is an ‘asymmetry’ at the first glance. The only notable secondary observation, which is peculiar, is that the crystallinity of the degassed CPM-37($Ni_{0.5}Fe_{2.5}$) is on par with the other mixed-metal samples or even slightly better than some of them, while the surface area is similar to the CPM-37(Fe). In this case the crystallinity turned out to be a poor indicator of the surface area, which is unexpected. It is not impossible that some pore entrances on the surface are closed as a result of partial collapse, while the major part of the structure withstands the collapse relatively well.

Section 2.10 Crystal structure of CPM-37(Ni)

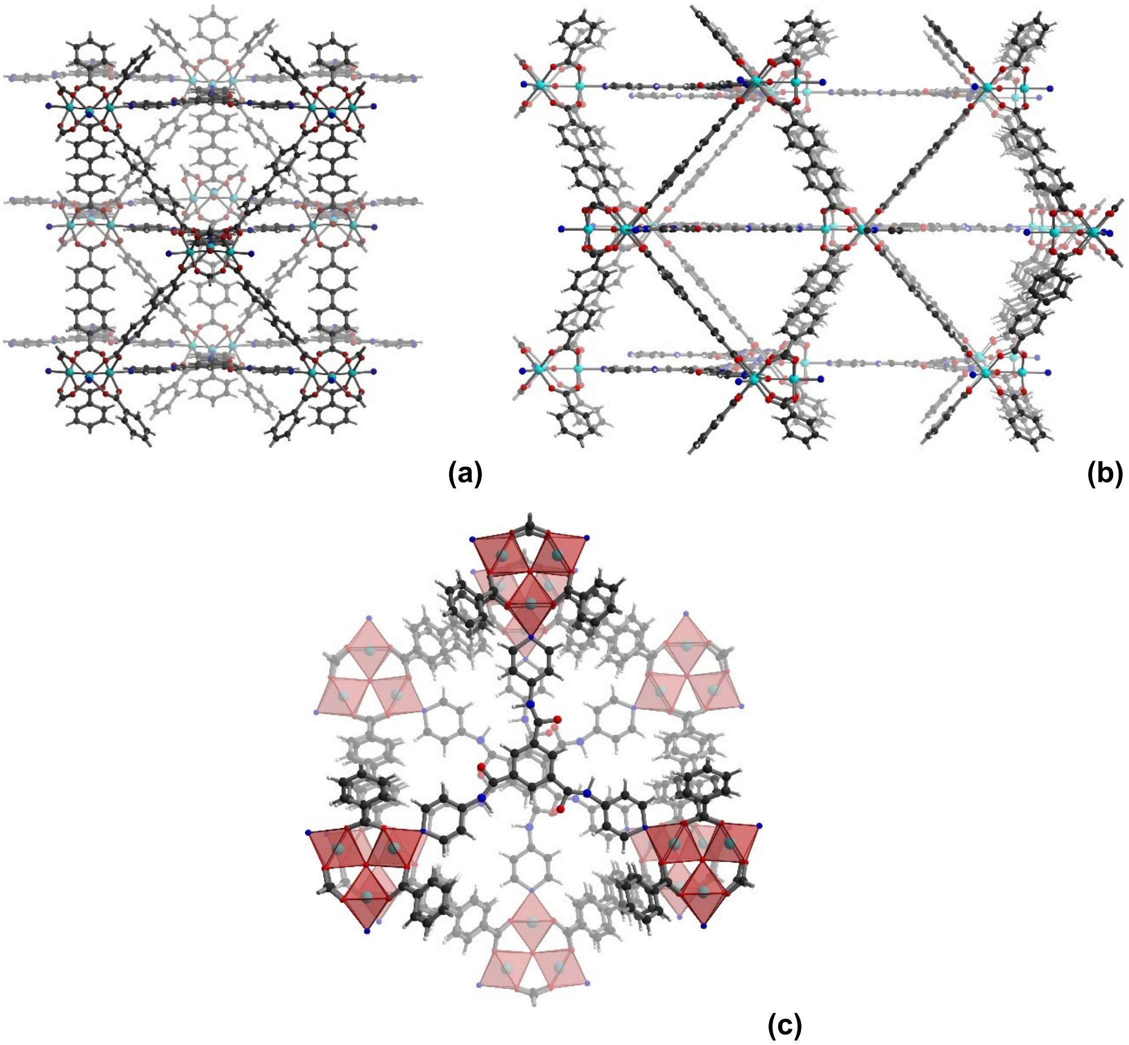

Fig. S20 Views on the CPM-37(Ni) structure:[25] a) along the (-110) direction demonstrating the pore-enclosures; b) the view on the structure along the *a*-axis with the well-visible triangular pore-channels; c) the view on the structure along the 6_3 axis.

Section 2.11 Electrochemical section

Section 2.11.1 Faradaic efficiency

To assess the Faradaic efficiency regarding oxygen generation, the method reported by Mascaros et al. was used,[26] using, in our case, a constant current of 50 mA cm^{-2}. The oxygen level in the electrochemical cell was monitored during the process using the Ocean Optics NeoFOX sensor system coupled with a FOSPOR probe. The FOSPOR probe was calibrated using a two-point method using nitrogen atmosphere (0% O_2) and in ambient air (21% O_2). The electrolyte was thoroughly freed from the initially dissolved oxygen by continuous bubbling of nitrogen gas for at least one hour before commencing the chronopotentiometric test.

The number of oxygen molecules produced during the electrolysis was determined using the subsequent formula, which assumes the applicability of the ideal gas law for the analysed gas mixture at atmospheric pressure:

$$n_{O2,exp} = x_{O2,frac}\, P_{total}\, V_{gas}\ \ R^{-1}\, T^{-1}$$

where $x_{O2,frac}$ is the fraction of oxygen in the evolved gaseous mixture as detected by the FOSPOR probe; P_{total} is the pressure of gas mixture (1 atm); V_{gas} (L) is the evolved gas volume at atmospheric pressure; R is the gas constant, 0.082 (atm L K^{-1} mol^{-1}); and T is the temperature (293 K).

The theoretical evolved Faradaic oxygen is given by:

$$n_{O2,far} = Q.n_e^{-1} F^{-1}$$

where, Q (measured in C, coulombs) represents the total electric charge transferred within the system; n_e signifies the molar amount of electrons for the production of one mole of oxygen (equals to 4), and F designates the Faraday constant (equal to 96485 C mol^{-1}). The Faradaic efficiency (expressed in percentage), denoted as FE, is determined using the following equation:

$$FE = \frac{n_{O2,exp}}{n_{O2,far}} * 100$$

Section 2.11.2 Comparison of the OER performance for different reported materials)

Table S14 Comparison of OER performance for the previously reported bimetallic nickel and iron MOF precatalysts and nickel-based catalysts in aqueous alkaline medium, KOH 1 mol L^{-1}, at 50 mA cm^{-2}.

Material	***η*** **(mV)**	**Tafel slope (mV dec^{-1})**	**Electrode type**	**Ref.**
CPM-37(Ni_2Fe)	290	39	NF	This work
NiSe@NiOOH	300	162	NF	27
Ni–Fe -MOF	270	49	NF	28
CD/$NiCo_2O_4$	390	91	NF	29
(Co/Ni/Cu) hydroxyphosphate	370	88	NF	30
Co_3O_4/$NiCo_2O_4$	407	84	NF	31
Porous Nickel–Iron Oxide	420	42	NF	32
FeNi-DOBDC	270	49	GC	28
$Ni(OH)_2$	330	140	NF	33
NiFeSe	300	80	NF	34
NiFeMoSe	253	36	NF	34
P-containing $NiCo_2S_4$	300	70	NF	35
Fe-Ni_3S_2	287	120	NF	36
NiCo-MOF	270	35.4	NF	37
Hierarchical Porous Ni_3S_4	300	40	NF	38
NCF/Ni-BDC	350	39.5	NF	39
Defective-CeO_2-x decorated MOF(Ni/Fe)	254	34	NF	40

References

---

1 S. Hasegawa, S. Horike, R. Matsuda, S. Furukawa, K. Mochizuki, Y. Kinoshita and S. Kitagawa, *J. Am. Chem. Soc.,* 2007, **129**, 2607–2614.
2 P. Maniam and N. Stock, *Inorg. Chem.,* 2011, **50**, 5085-5097.
3 C. R. Wade and M. Dincă, *Dalton Trans.,* 2012, **41**, 7931-7938.
4 Y. Li, A. Hammoud, L. Bouteiller and M. Raynal, *J. Am. Chem. Soc.,* 2020, **142**, 5676−5688.
5 K. I. HadjiivanoV, D. A. Panayotov, M. Y. Mihaylov, E, Z. Ivanova, K. K. Chakarova, S. M. Andonova and N. L. Drenchev, *Chem. Rev.,* 2021, **121**, 1286−1424.
6 Y. Wu, X. Song, S. Li, J. Zhang, X. Yang, P. Shen, L. Gao, R. Wei, J. Zhang and G. Xiao, *J. Ind. Eng. Chem.,* 2018, **58**, 296-303.
7 O. M. Yaghi, H. Li, and T. L. Groy, *J. Am. Chem. Soc.,* 1996, **118**, 9096–9101.
8 A. Modrow, D. Zargarani, R. Herges and N. Stock, *Dalton. Trans.,* 2012, **41**, 8690-8696.
9 F. Israr, D. Chun, Y. Kim and D. K. Kim, *Ultrason. Sonochem.,* 2016, **31**, 93-101.
10 C. Lucarelli, S. Galli, A. Maspero, A. Cimino, C. Bandinelli, A. Lolli, J. V. Ochoa, A. Vaccari, F. Cavani and S. Albonetti, *J. Phys. Chem. C.,* 2016, **120**, 15310–15321.
11 A. Awadallah, F. Hillman, S. A. Al-Muhtaseb and H-K. Jeong, *J. Mater. Sci.,* 2019, **54**, 5513–5527.
12 G. T. Vuong, M. H. Phama and T-O. Do, *CrystEngComm,* 2013, **15**, 9694-9703.
13 X. Zheng, L. Zhang, Z. Fan, Y. Cao, L. Shen, C. Au and L. Linag, *J. Chem. Eng*., 2019, **374**, 793–801.
14 D. S. Hall, D. J. Lockwood, C. Bock and B. R. MacDougall, *Proc. R. Soc. A.,* 2015, **471**, 20140792.
15 C.W. Hu, Y. Yamada and K. Yoshimura, *J. Mater. Chem. C.,* 2016, **4**, 5390-5397.
16 S. Abelló, F. Medina, D. Tichit, J. P. Ramírez, J. C. Groen, J. E. Sueiras, P. Salagre and Y. Cesteros, *Eur. J. Chem.,* 2005, **11**, 728-739.
17 F. B. D. Saiah, B.L. Su and N. Bettahar, *J. Hazard. Mater.,* 2009, **165**, 206-217.
18 M. C. Biesingera, B. P. Payne, A. P. Grosvenord, L. W. M. Lau, A. R. Gerson and R. S. C. Smart, *Appl. Surf. Sci*., 2011, **257,** 2717-2730.
19 L. Zhou, Z. Niu, X. Jin, L. Tang and L. Zhu, *ChemistrySelect,* 2018, **3**, 12865–12870.
20 J. Zhou, Z. Han, X. Wang, H. Gai, Z. Chen, T. Guo, X. Hou, L. Xu, X. Hu, M. Huang, S. V. Levchenko and H. Jiang, *Adv. Funct. Mater.,* 2021, **31**, 2102066.
21 R.J.J. Jansen and H. V. Bekkum, *Carbon*,1995, **33**, 1021-1027.
22 A. Punnoose, K. Dodge, J. J. Beltrán, K. M. Reddy, N. Franco, J. Chess, J. Eixenberger and C. A. Barrero, *J. Appl. Phys*. 2014, **115**, 2012-2015.
23 Q. Li, G. Li, C. Fu, D. Luo, J. Fan and L. Li, *ACS Appl. Mater. Interfaces,* 2014, **6**, 13, 10330–10341.

24 S. Abdpour, L. Rademacher, M. N. A. Fetzer, T. H. Y. Beglau and C. Janiak, *Solids,* 2023, **4**, 181–200.
25 X. Zhao, X. Bu, Q. Zhai, H. Tran, and P. Feng, *J. Am. Chem. Soc.,* 2015**, 137**, 1396−1399.
26 J.Yu, S.Giancola, B. Khezri, D.N. Castro, J. Redondo, F. Schiller, S. Barja, M. C. Spadaro, J. Arbiol, F.A. Garce´s-Pineda, and J. R. G. Mascaro´s, *EES Catal.,* 2023, **1**, 765.
27 X. Li, G.-Q. Han, Y.-R. Liu, B. Dong, W.-H. X. Y.-M. Chai and C-G. Liu, *ACS Appl. Mater.Interfaces,* 2016, **8**, 20057–20066.
28 F. Zheng, D. Xiang, P. Li, Z. Zhang, C. Du, Z. Zhuang, X. Li and W. Chen, *ACS Sustain. Chem. Eng.,* 2019**, 7**, 9743–9749.
29 A. Kundu, B. Ryplida and S. Y.Park, *Electroanalysis,* 2020, **32**, 2090–2100.
30 Y. Zhang, T. Qu, F. Bi, P. Hao, M. Li, S. Chen, X. Guo, M. Xie and X. Guo, *ACS Sustain. Chem. Eng.,* 2018, **6**, 16859–16866.
31 M. Yang, W. Lu, R. Jin, X.-C, Liu, S. Song and Y. Xing, *ACS Sustain. Chem. Eng.,* 2019, **14**, 12214–12221.
32 J. Qi, W. Zhang, R. Xiang, K. Liu, H.-Y. Wang, M. Chen, Y. Han and R. Cao, *Adv. Sci*., 2015, **2**, 1500199.
33 Y. Rao, Y. Wang, H. Ning, P. Li and M. Wu, *ACS Appl. Mater. Interfaces,* 2016, **8**, 33601–33607.
34 Z. Yin, J. Liang, H. Xu, H. Luo, D. Deng, W. Luand and S. Long *J. Electroanal. Chem.,* 2021, **895**, 115501.
35 K. Min, R. Yoo, S. Kim, H. Kim, S.E. Shim, D. Lim and S.-H. Baeck, *Electrochim. Acta*., 2021, **396**,
36 Y. Yang, F. Guo, L. Zhang, X. Guo, D. Wang, R. Niu, H. Yang, J. Li, G. Ma and Z. Lei, *Dalton Trans.,* 2022, **51**, 17283-17291.
37 P. Thangasamy, S. Shanmuganathan and V. Subramanian, *Nanoscale Adv.,* 2020, **2**, 2073-2079.

---

38 K. Wan, J. Luo, C. Zhou, T. Zhang, J. Arbiol, X. Lu, B.-W. Mao, X. Zhang and J. Fransaer, *Adv. Funct. Mater.,* 2019, **29**, 1900315.

39 E. Sadeghi, N.S. Peighambardoust, S. Chamani and U. Aydemir, *ACS Mater. Au,* 2023, **3**, 143–163.

40 M. Wu, Y. Zhang, R. Zahng, J. Ma and N. A. Vante, *Electrochim. Acta.,* 2022, **403**, 139630.